AIAA JOURNAL
Vol. 39, No. 5, May 2001

Vortex Breakdown–Edge Interaction: Consequence of Edge Oscillations

B. Sahin* and H. Akilli†
Cukurova University, Balcali, 01330 Adana, Turkey
and
J.-C. Lin‡ and D. Rockwell§
Lehigh University, Bethlehem, Pennsylvania 18015

High-image-density particle image velocimetry is employed to determine the instantaneous and averaged features of distortion of vortex breakdown incident on a stationary and an oscillating leading edge. It is demonstrated that the onset of vortex breakdown can be advanced or retarded substantially, depending on the period of the edge oscillation relative to the inherent frequency of vortex breakdown. These features are interpreted with the aid of global representations of averaged and rms distributions of velocity, vorticity, and Reynolds stress, as well as a cinema sequence of instantaneous patterns of velocity and vorticity. Moreover, instantaneous, whole-field images in a cinema sequence allow evaluation of global representations of spectra and cross spectra, providing further insight into the central mechanisms that dictate the surface loading of the edge.

Nomenclature

C	=	chord of delta wing, mm
D_v	=	characteristic vortex diameter, mm
f	=	frequency, Hz
f_e	=	excitation frequency of edge of plate, Hz
f_N	=	Nyquist frequency, Hz
f_0	=	frequency of vortex breakdown, Hz
L_p	=	length of plate, mm
M	=	magnification
N	=	number of samples
Re	=	Reynolds number, $U_\infty C/\nu$
S_{ab}	=	magnitude of cross spectrum
T	=	total sampling time, s
T_e	=	period of edge oscillation, s
T_0	=	period of inherent (undisturbed) vortex breakdown, s
U_{ref}	=	reference velocity, U_∞, mm/s
U_∞	=	freestream velocity, mm/s
u	=	horizontal component of velocity, mm/s
$u'v'$	=	Reynolds stress correlation
V	=	total velocity, mm/s
X_b^*	=	vortex breakdown location in presence of edge oscillations, mm
$(X_b^*)_0$	=	vortex breakdown location for stationary plate, mm
α	=	angle of attack of delta wing, deg
α_p	=	angle of attack of plate, deg
Γ	=	circulation of the vorticity concentration, mm^2/s
ΔS	=	distance between two points for cross-spectrum evaluation
Δt	=	sampling time, s
Λ	=	sweep angle of delta wing, deg
ϕ_{ab}	=	phase shift of cross spectrum
ω	=	vorticity, s^{-1}
ω_{rms}	=	root mean square of vorticity fluctuation, s^{-1}

Introduction

BUFFETING of aircraft tails or fins by a broken-down vortex, which has its origin at an aerodynamic surface located upstream, represents an important class of flow–structure interaction that can give rise to vibration, and potentially failure, of the tail or fin. This class of vortex–body interactions is part of a broader range of interaction phenomena, as recently reviewed by Rockwell.[1] Experimentally based investigations have provided valuable information on the loading and response characteristics of the tail (or fin), sometimes accompanied by qualitative flow visualization. In recent years, a major emphasis, from an experimental standpoint, has focused on various combinations of the time-averaged and unsteady forces, moments, and surface pressures, and surface acceleration as addressed in the works of Triplett,[2] Brown et al.,[3] Lee et al.,[4] and Lee and Brown.[5] A summary of recent investigations, including efforts to control buffeting, is provided by Huttsell et al.[6]

Of course, all of these features of the unsteady loading and acceleration have their genesis in the vortical flow patterns impinging upon the fin or tail. Flow visualization of the vortex structure is provided by Erickson et al.[7] and Fisher et al.[8] (also see closely related study by Del Frate et al.[9]). The velocity fluctuation fields in the vicinity of vertical tails, induced by the incident vortex, have been addressed in several investigations. Sellers et al.[10] performed measurements on a model of a YF-17 aircraft and demonstrated the occurrence of large velocity fluctuations in the vicinity of the tails. Komerath et al.[11,12] considered a model of an F-15 aircraft and showed occurrence of peaks in the velocity spectra, at locations both inboard and outboard of the vertical tails, at high angle of attack. Breitsamter and Laschka[13] provide extensive data of the pointwise-averaged velocity field in the vicinity of a fin region of a delta-canard configuration. Despite the Reynolds number being relatively high, that is, $Re = 10^6$, spectra of the velocity field exhibited sharply defined peaks. These observations confirm the essentially inviscid nature of the fluctuating field due to vortex breakdown and are in accord with a visualized spiral instability of vortex breakdown on a full-scale research version of the F-18 aircraft at high angle of incidence, performed by Fisher et al.[8]

Global, quantitative characterization of the flow is required for an adequate understanding of these phenomena. Imaging of vortex–plate and vortex–tail interactions, providing both global instantaneous and time-averaged information is described by Mayori and Rockwell,[14] Canbazoglu et al.,[15] and Wolfe et al.[16] These investigations of vortex breakdown–surface interactions provide an essential foundation for the investigations proposed herein. An alternate type of imaging approach, involving planar Doppler velocimetry, has yielded time-averaged representations of vortex–fin interaction. Global images of selected parameters, in root-mean-square form, are given by Beutner et al.[17]

Numerical investigations of Rizk and Gee,[18] Gee et al.,[19] Kandil et al.,[20] and Rizzetta[21] have simulated various aspects of the vortex

Received 1 November 1999; revision received 13 October 2000; accepted for publication 17 October 2000.

*Professor, Department of Mechanical Engineering.
†Assistant Professor, Department of Mechanical Engineering.
‡Research Associate, Department of Mechanical Engineering.
§Paul B. Reinhold Professor, Department of Mechanical Engineering and Mechanics. Member AIAA.

breakdown–tail interaction in relation to the loading characteristics. Among other features pointed out by these numerical investigations, the importance of upstream influence of aeroelastic deflections of the tail on the onset of vortex breakdown has been addressed by Kandil et al.[20] Computations by Gordnier and Visbal[22,23] provide a detailed description of the instantaneous and time-averaged three-dimensional flow structure generated by the impingement of a delta wing vortex pair on a plate. Their study revealed the existence of complex separation patterns on both sides of the plate resulting from the spanwise variation in effective angle of attack, which is induced by the incoming vortex system. The vortex breakdown location was found to be sensitive to the degree of obstruction created by the stall on the plate. This mutual interaction between the incident vortex breakdown and the separated flow on the impingement surface may provide a basis for future flow control strategies.

The foregoing numerical and experimental investigations recognize the existence of a predominant spectral peak, that is, predominant frequency component above the broadband background, due to vortex breakdown. It has important consequences for loading of the tail. This predominant frequency corresponds to the helical mode instability of the flow downstream of the onset of vortex breakdown as addressed by Garg and Leibovich[24] and Gursul.[25] Wolfe et al.[26] showed that dominant frequencies of surface pressure fluctuations on fins agree very well with those on the surface of delta wings without a fin characterized by Gursul.[25] Wolfe et al.[26] propose a simple scaling parameter for the dominant frequency, valid over a wide range of Reynolds and Mach numbers. This relationship is further substantiated by Wolfe et al.[16] for the limiting case of direct and near-direct encounter of a broken-down vortex with a flat plate. In this investigation, pressure spectra on the plate were compared with the instantaneous structure of the incident vortex. It was shown that the dominant frequency of loading is relatively insensitive to the offset of the incident vortex. Moreover, the largest amplitude loading occurs when the maximum mean vorticity of the incident vortex is aligned with the leading edge of the plate.

The objective of this investigation is to characterize the interaction of vortex breakdown with stationary and oscillating leading edges using a global imaging technique. The possibility of retardation or advancement of the process of vortex breakdown, the nature of local vorticity–edge interactions, and the coupling between the flow patterns in the vicinity of the tip of the edge and the upstream development of vortex breakdown will be addressed. Moreover, spectral and cross-spectral analysis using a sequence of instantaneous, global images will be undertaken to determine spectral features of the incident vortex and the distorted vorticity field past the edge, which in turn dictate the unsteady loading on the edge.

Experimental System and Techniques

Experiments were performed in a large-scale water channel having a test section length of 4928 mm, a width of 927 mm, and a height of 610 mm. During the course of the experiments, the water level was maintained at 559 mm, which prevented overflow of the channel, especially during startup of the pump. The freestream velocity U_∞ was 45 mm/s, giving a value of Reynolds number based on wing chord C of 1.024×10^4.

As shown in Fig. 1, a leading-edge vortex, which was generated from a delta wing, impinged on a plate having a sharp leading edge. The angle of attack of the delta wing was $\alpha = 24$ and 30 deg for the present experiments; unless otherwise noted, $\alpha = 24$ deg. The plate had an angle of attack of $\alpha_p = 0$ and 2.5 deg. The delta wing had a chord $C = 222$ mm and a sweep angle $\Lambda = 75$ deg. The thickness of the wing was 3.18 mm. It was beveled at an angle of 34 deg on its windward side. The plate had a length $L_p = 162$ mm and a thickness $t_p = 6.35$ mm; its leading and trailing edges were beveled at angles of 5 and 12 deg, respectively. The distance between the trailing edge of the delta wing and the leading edge of the plate was maintained at $L = 73$ mm. The onset of vortex breakdown occurred a distance X_b^* upstream of the leading edge of the plate. For the case of the stationary edge, the breakdown occurs at $(X_b^*)_0$.

The plate was subjected to prescribed pitching oscillations about its midchord by a high resolution stepping motor, which was controlled by the laboratory microcomputer. The impingement plate extends along the entire span of the test section. The variation of angle of attack is defined as $\alpha_p(t) = \bar{\alpha}_p + (\alpha_p)_0 \sin \omega_e t$, in which $\omega_e = 2\pi f_e$. Unless otherwise indicated, $\bar{\alpha}_p = 0$ and $(\alpha_p)_0 = 2.5$ deg for all experiments. This pitching amplitude of the plate corresponds to a tip displacement of ± 3.5 mm, relative to the vortex diameter of 8.5 mm. The period $T_e = 2\pi/\omega_e$ was varied over the interval $1 \le T_e \le 6$ s, relative to the period $T_0 = 1.66$ s of the inherent frequency of vortex breakdown in the spiral mode. At $T_e = 1$ s, the vortex patterns induced at the leading edge dominated the vortex–plate interaction, thereby providing a reasonable lower limit of T_e.

Instantaneous images of the vortex breakdown–edge interaction were acquired using a technique of high-image-density particle image velocimetry (PIV), described by Rockwell et al.[27] The beam from a continuous wave argon-ion laser was transmitted through an optical train, then impinged upon a rotating multifaceted (48) mirror, to generate a scanning laser sheet. This sheet is indicated by the

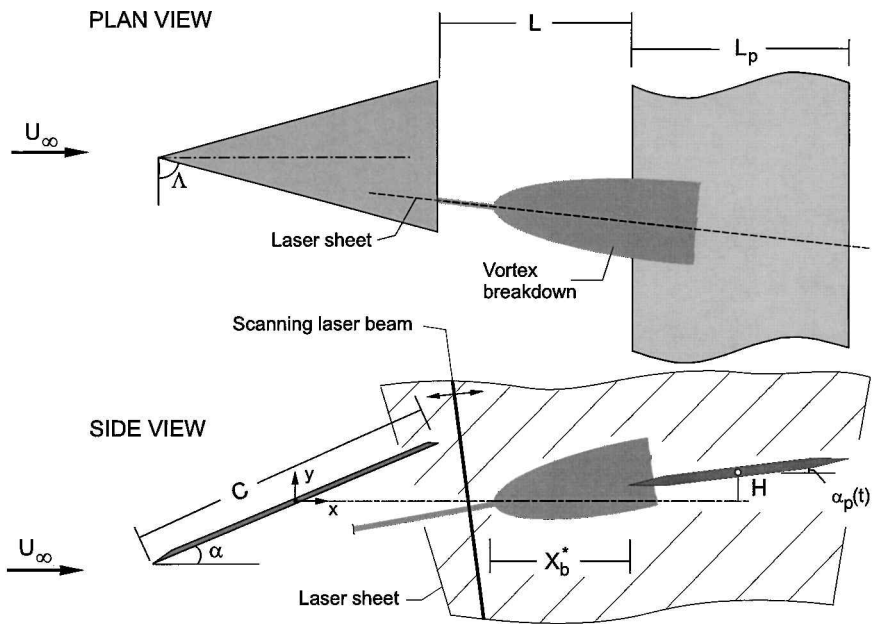

Fig. 1 Plan and side views of experimental system where delta wing is stationary and impingement plate oscillates according to $\alpha_p(t) = \bar{\alpha}_p + (\alpha_p)_0 \sin \omega_e t$.

bold dashed line in the plan view of Fig. 1. It was aligned with the centerline of the leading-edge vortex. The scanning frequency was adjusted to 75 Hz. To provide well-defined particle images for the PIV technique, the flow was seeded with 14.6-μm metallic-coated hollow plastic spheres. At the aforementioned value of laser scanning frequency, typically four to five multiple exposures of each particle image were acquired during each shutter opening of the camera. These particle images were recorded on 35-mm high-resolution film having 300 lines/mm as specified by the manufacturer. The patterns of particle images were digitized at a resolution of 125 pixels/mm. The mean diameter of each particle image was 0.4 pixels (3.26 μm). A single-frame cross-correlation technique was employed to determine the velocity field. The interrogation window had a size of 1.55×1.55 mm (90×90 pixels) in the plane of the laser sheet. Because the magnification was $M = 1:4.3$, the size of the interrogation window on the film was 0.36×0.36 mm. To satisfy the Nyquist criterion, a 50% overlap was used during the interrogation process. Moreover, to ensure that the high-image-density criterion was satisfied, each interrogation window contained a total of approximately 40–60 particle images. Cinema representations of the flow were obtained by employing the maximum framing rate (5.55 frames/s) of the 35-mm camera.

Calculation of the averaged quantities was performed according to the equations defined in the following. Each averaged parameter was determined at each spatial coordinate (x, y) by considering the average of all instantaneous values (x, y). The terminology and definition of each of the averaged parameters are as follows:

$\langle V \rangle$ is the averaged (or mean) total velocity,

$$\langle V \rangle \equiv \frac{1}{N} \sum_{n=1}^{N} V_n(x, y) \tag{1}$$

$\langle u \rangle$ is the averaged value of horizontal component of velocity,

$$\langle u \rangle \equiv \frac{1}{N} \sum_{n=1}^{N} u_n(x, y) \tag{2}$$

$\langle \omega \rangle$ is the mean value of vorticity ω,

$$\langle \omega \rangle \equiv \frac{1}{N} \sum_{n=1}^{N} \omega_n(x, y) \tag{3}$$

ω_{rms} is the root mean square of vorticity fluctuation,

$$\omega_{\text{rms}} \equiv \langle \omega \rangle_{\text{rms}} \equiv \left[\frac{1}{N} \sum_{n=1}^{N} [\omega_n(x, y) - \langle \omega(x, y) \rangle]^2 \right]^{\frac{1}{2}} \tag{4}$$

and $\langle u'v' \rangle$ is the averaged value of Reynolds stress correlation,

$$\langle u'v' \rangle \equiv \frac{1}{N} \sum_{N=1}^{n} [u_n(x, y) - \langle u(x, y) \rangle][v_n(x, y) - \langle v(x, y) \rangle] \tag{5}$$

The effect of the number of images on the foregoing averages was examined and is described subsequently in the subsection "Averaged Flow Patterns."

Using the cinema sequence of instantaneous images, it was possible to construct, at arbitrary locations in the flow, the time history of velocity and vorticity and then to evaluate the spectrum and cross-spectrum using approaches similar to those employed for classical pointwise measurement techniques. The associated parameters and the limitations of the calculated values are described in the subsection "Spectra and Cross Spectra Based on Instantaneous Imaging of Vortex Breakdown–Edge Interaction." The Nyquist frequency was $f_N = 2.78$ Hz.

Vortex Breakdown–Edge Interactions

Averaged Flow Patterns

Figure 2 shows the location of the onset of vortex breakdown X_b^* due to edge oscillations. The angle of attack of the delta wing is $\alpha = 24$ deg. The mean and fluctuating angle of attack of the impingement plate are $\bar{\alpha}_p = 0$ deg and $(\bar{\alpha}_p)_0 = 2.5$ deg, respectively, where $\alpha_p(t) = \bar{\alpha}_p + (\alpha_p)_0 \sin \omega_e t$. The value of X_b^* was determined from dye injection; it corresponded to an abrupt increase in the visualized cross section of the vortex. For each period T_e of the plate excitation, six dye images were recorded on a video system, and the locations of vortex breakdown were averaged to yield a single value of X_b^*. In Fig. 2, X_b^* is normalized by $(X_b^*)_0$, which represents the onset of breakdown for the stationary edge. This parameter is a function of the period T_e of the edge oscillation normalized by the period T_0 of the spiral mode instability of vortex breakdown during its interaction with the stationary edge, T_e/T_0. The circular data points indicate averaged data, and the vertical bars represent the maximum deviation of the self-excited excursions about these averaged values. At small values of $T_e/T_0 \cong 0.25$, the onset of vortex breakdown is substantially advanced upstream as the ratio $X_b^*/(X_b^*)_0$ approaches a value of 2. As indicated by the magnitude of the vertical bars for $T_e/T_0 \cong 0.25$, substantial instantaneous excursions occur about the averaged location of the vortex breakdown. On the other hand, at larger values of T_e/T_0, the onset of breakdown is remarkably retarded over a range of excitation, $1 \leq T_e/T_0 \leq 2.5$. At sufficiently high values of T_e/T_0, the location of onset of vortex breakdown approaches its value corresponding to the stationary edge; this limiting case represents a quasi-steady response. The physical basis for the advancement and retardation of the onset of vortex breakdown is addressed in the averaged and instantaneous images that follow.

Figure 3a shows contours of constant $\langle u \rangle / U_{\text{ref}}$ for a range of oscillation T_e of the edge, relative to those of the stationary edge. The

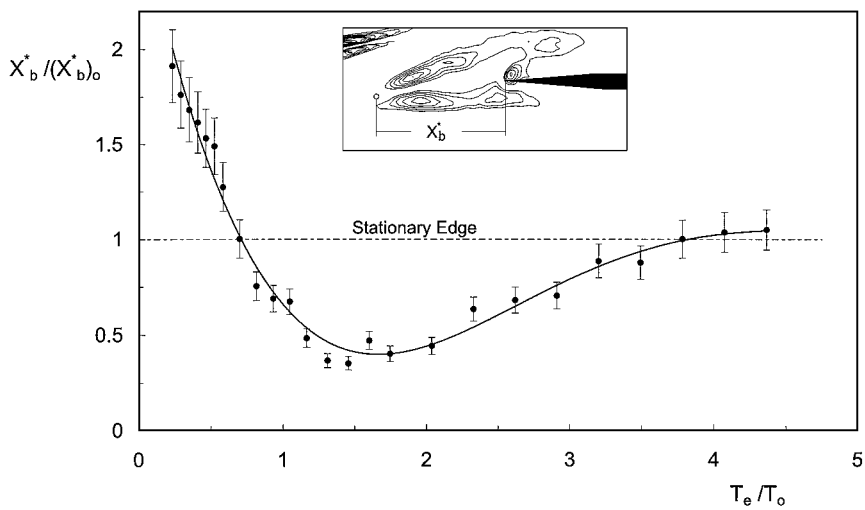

Fig. 2 Averaged location of onset of vortex breakdown as a function of dimensionless period of oscillation of impingement plate.

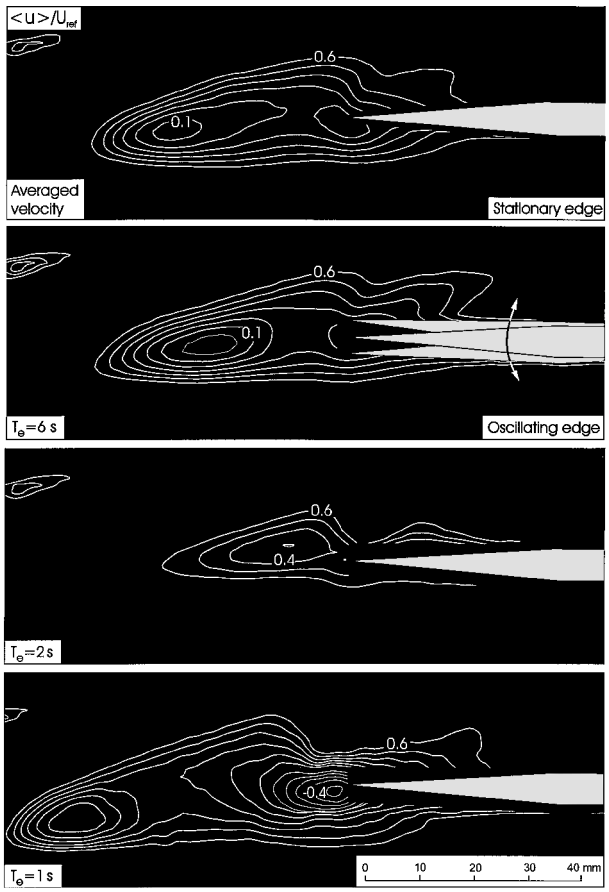

Fig. 3a Contours of constant averaged streamwise velocity $\langle u \rangle$ normalized by reference velocity U_{ref} for the case of a stationary edge and an edge oscillating at defined period T_e.

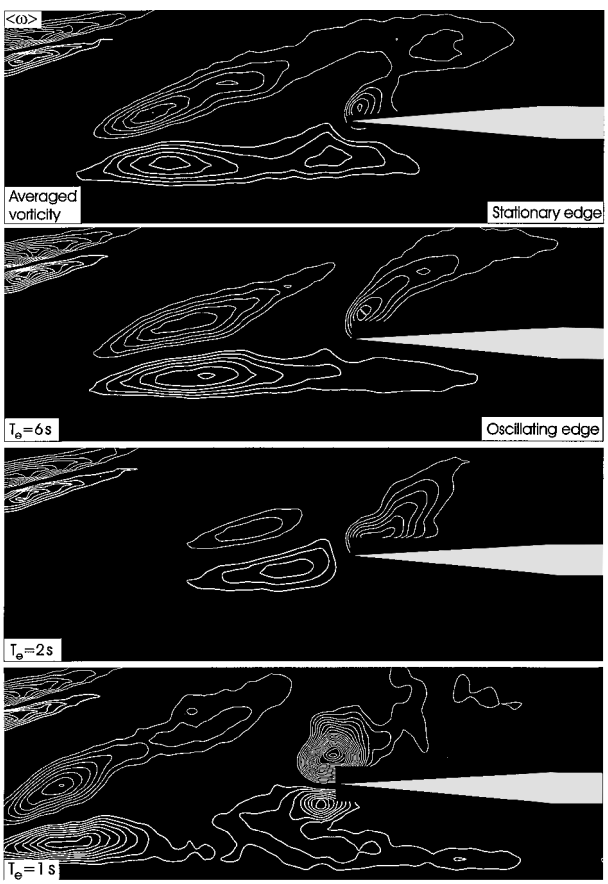

Fig. 3b Contours of constant averaged vorticity $\langle \omega \rangle$ for the case of the stationary edge and an edge oscillating at prescribed period T_e.

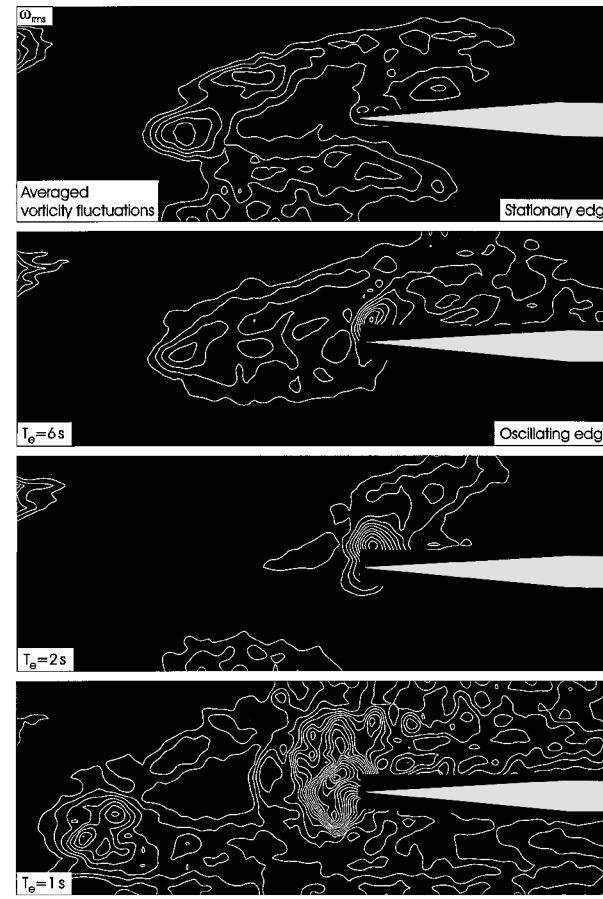

Fig. 3c Contours of constant fluctuating vorticity ω_{rms} for stationary edge and edge oscillating at defined T_e.

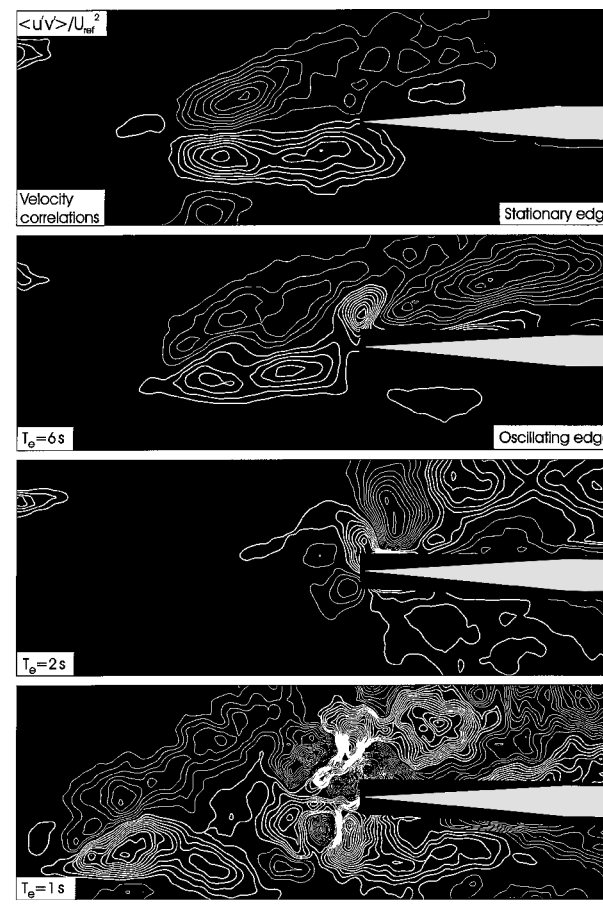

Fig. 3d Contours of constant $\langle u'v' \rangle / U_{\text{ref}}^2$ for a stationary edge and an edge oscillating at defined values of period T_e.

averaged component of streamwise velocity $\langle u \rangle$ is normalized with respect to the reference velocity $U_{\text{ref}} = U_\infty$ at a location in the relatively undisturbed region of the flow. For Fig. 3a, $\langle u \rangle$ corresponds to a location $x/C = 0.5$ and $y/C = 0.65$; these coordinates are defined in Fig. 1. In Fig. 3a, the maximum contour level of $\langle u \rangle / U_{\text{ref}} = 0.6$ corresponds to the outermost contour; successive contours lying within this outer one correspond to incrementally decreasing values of positive $\langle u \rangle / U_{\text{ref}} = 0.1$; each is represented by a thick white line. Negative values of $\langle u \rangle / U_{\text{ref}}$ are observed in parts of Fig. 3a; they are represented by the thin white line. When Fig. 3a is viewed as a whole, it is evident that a wakelike region exists upstream of the leading edge. At locations downstream of the tip of the edge, contours of $\langle u \rangle / U_{\text{ref}}$ tend to merge along the surface of the edge. The bubblelike depictions of the wake regions of Fig. 3a all show the existence of a well-defined minimum immediately downstream of the leading edge of the bubble. Moreover, for the case of the lowest period of excitation $T_e = 1$ s, a negative pocket of $\langle u \rangle / U_{\text{ref}}$ is nearly centered at the tip of the edge. For this extreme case, the leading edge of the bubble protrudes the farthest distance upstream. Note that the aforementioned effects of retardation and advancement of the onset of vortex breakdown were also clearly evident in the dye visualization described in conjunction with Fig. 2. Such visualization provides, of course, a fully three-dimensional portrayal of the modified breakdown.

Figure 3b provides a parallel set of images corresponding to contours of constant averaged vorticity $\langle \omega \rangle$ where minimum and incremental values of $\langle \omega \rangle$ are ± 2 and 0.75 s^{-1}. These images show well-defined concentrations of positive (thick white line) and negative (thin white line) azimuthal vorticity upstream of the leading edge. The transverse distance between the extrema of positive and negative vorticity on either side of the region of vortex breakdown is defined as the characteristic diameter D_v of the broken-down vortex. The leftmost boundaries of these vorticity contours, that is, the leading edges of the vorticity contour plots, are taken to define the onset of vortex breakdown, which is designated as the streamwise location of the minimum vorticity contour. This location is approximately coincident with the outermost contour of $\langle u \rangle / U_{\text{ref}} = \langle u \rangle / U_\infty$ exhibited in Fig. 3a, which represents the edge of the wake-like region of vortex breakdown. Moreover, at the tip of the edge, a vorticity layer is formed in parts of Fig. 3b, due to the finite angle of attack α_p of the leading edge of the plate with respect to the axis of the vortex. At sufficiently low values of excitation period $T_e = 1$ s, highly concentrated vortices are evident on both the upper and lower sides of the leading edge. Finally, note that remnants of the pattern of vorticity formed in the wake of the delta wing are evident in the upper left corner of each image.

When the entire layout of Fig. 3b is viewed, it is evident that the pattern of vorticity at the excitation condition $T_e = 6$ s is very similar to that of the corresponding to the stationary edge, suggesting that an essentially quasi-steady perturbation of the vortex and its interaction with the edge are attained. This case corresponds to a ratio $T_e/T_0 = 3.5$ (compare Fig. 2). When the excitation period is lowered to $T_e = 2$ s, corresponding to $T_e/T_0 = 1.2$, the onset of vortex breakdown is substantially retarded, that is, it moves downstream toward the tip of the edge. Moreover, the peak values of vorticity in the vortex breakdown region are dramatically reduced. The converse situation occurs for $T_e = 1$ s, that is, $T_e/T_0 = 0.6$, for which the onset of breakdown is substantially advanced in the upstream direction. Moreover, the peak values of vorticity in the breakdown region are increased significantly relative to those for the case of a stationary edge. Remarkably high levels of peak positive and negative vorticity are generated along the upper and lower surfaces of the edge.

Figure 3c shows contours of root-mean-square vorticity fluctuation ω_{rms} (corresponding to the images of Fig. 3b) where minimum and incremental values of ω_{rms} are 1.5 and 0.5 s^{-1}. For the cases of

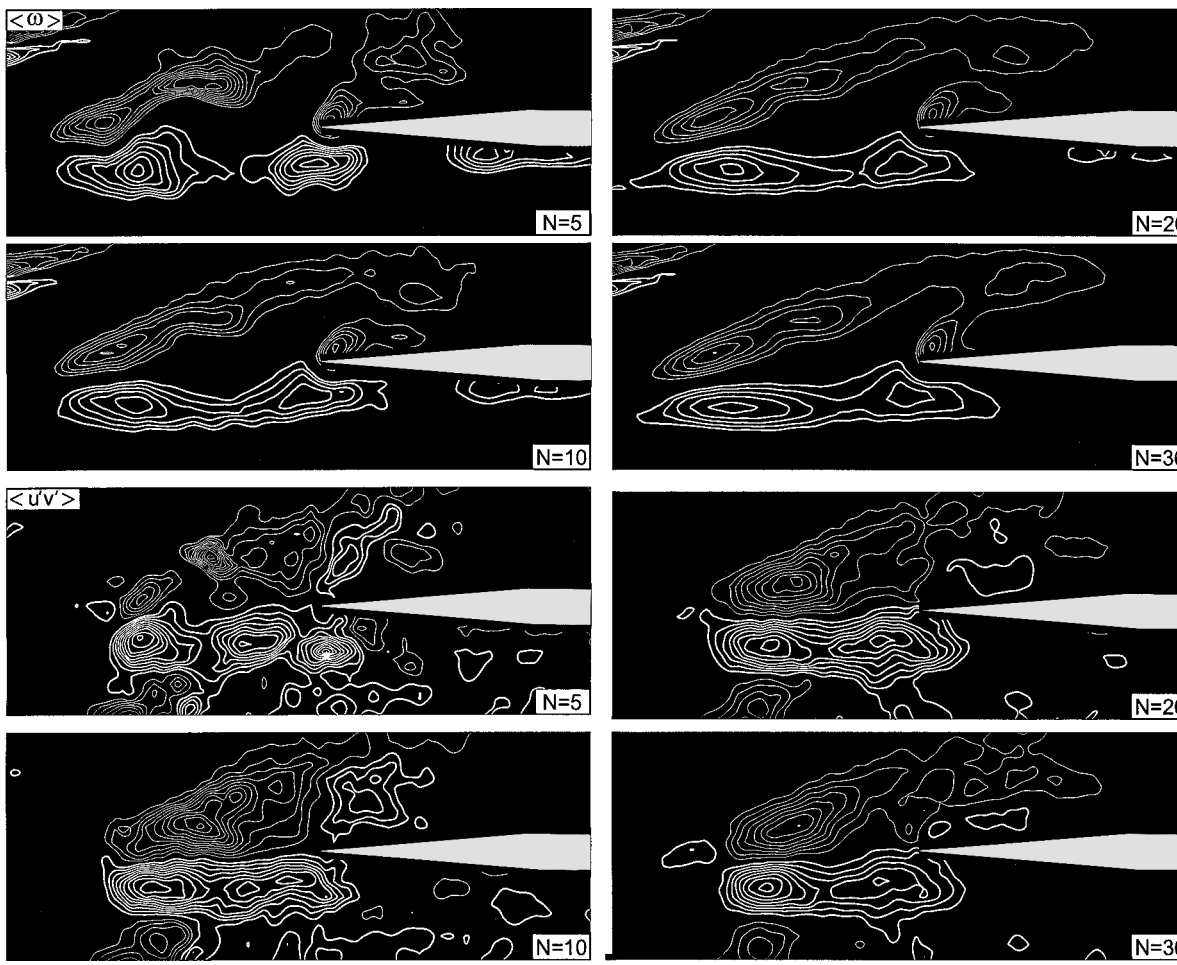

Fig. 3e Effect of number N of instantaneous images on averaged vorticity $\langle \omega \rangle$ and velocity $\langle u' v' \rangle$ for the case of the stationary plate.

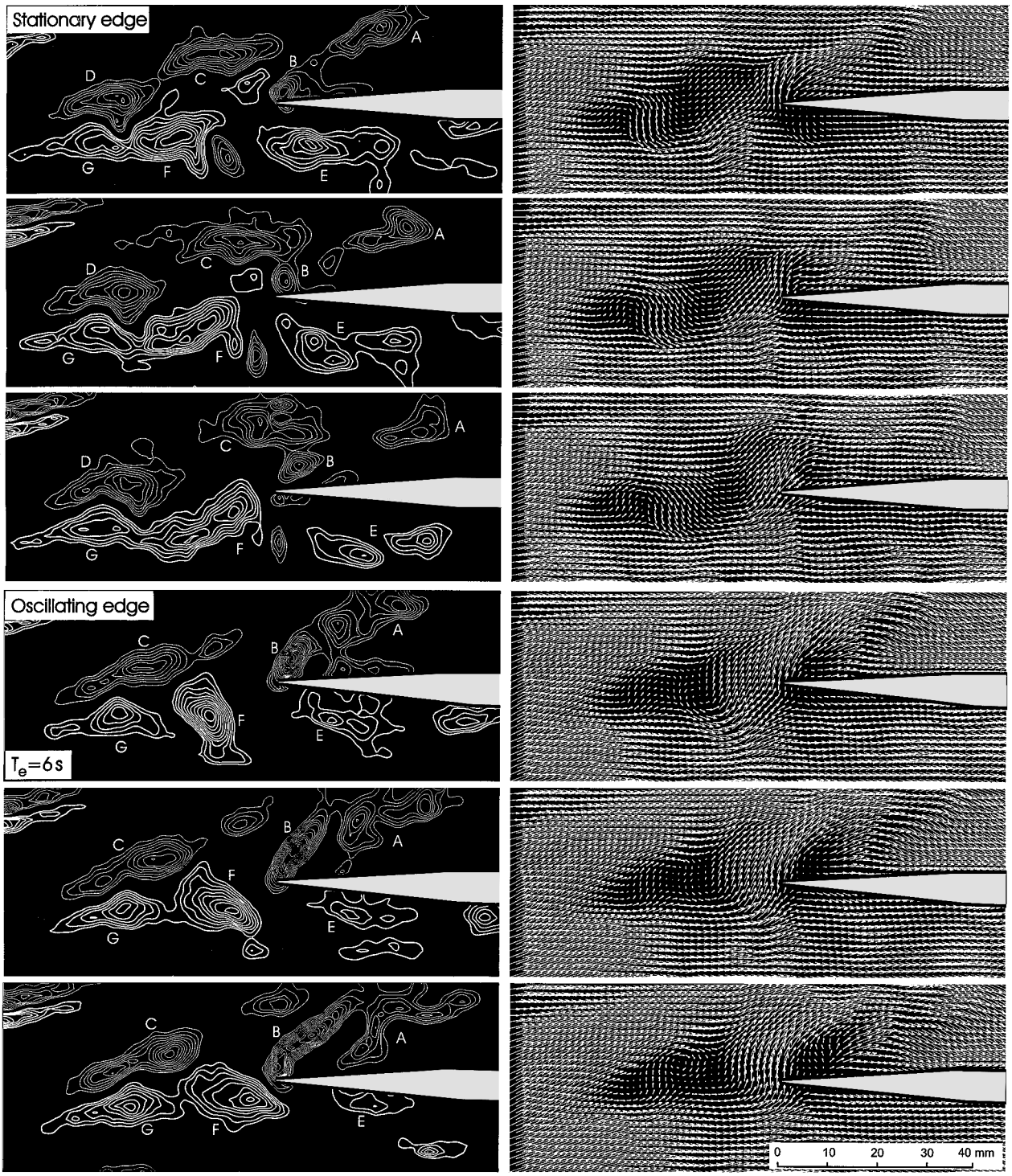

Fig. 4a Excerpts from cinema sequences showing patterns of instantaneous vorticity and distributions of velocity vectors for the case of a stationary edge and an edge oscillating at $T_e = 6$ s.

the stationary edge and the edge oscillating at $T_e = 6$ s, an extremum of ω_{rms} occurs at a location along the centerline of the region of vortex breakdown. This extremum is, however, displaced upstream of the locations of the peak value, that is, extremum of $\langle\omega\rangle$ shown in Fig. 3b. This extremum is located in the shear layers of the breakdown bubble. Moreover, the maximum values of ω_{rms} appear to occur at or near the maximum negative value of $\langle u\rangle/U_{\text{ref}}$, that is, within the region of substantial velocity defect in the wakelike region of the breakdown bubble, as shown in Fig. 3a. Furthermore, a distinctive feature of the vorticity pattern upstream of the stationary edge is the occurrence of vorticity fluctuations occurring in two distinct layers, one above and the other below the edge. On the other hand, no such bifurcation of the ω_{rms} contours occurs for the edge oscillation at $T_e = 6$ s. Figure 3c also shows that, at $T_e = 2$ s, the breakdown process is markedly retarded; significant levels of ω_{rms} do not occur upstream of the tip of the edge. Rather, relatively high values of ω_{rms} occur in the vicinity of the tip, due to its oscillation. Finally, substantially enhanced levels of ω_{rms} in the initial region of vortex breakdown, as well as in the vicinity of the tip of the edge, are evident at the lowest excitation period $T_e = 1$ s.

Corresponding values of the averaged velocity correlation $\langle u'v'\rangle U_{\text{ref}}^2 = \langle u'v'\rangle/U_\infty^2$ are shown in Fig. 3d. Minimum and incremental values of $\langle u'v'\rangle/U_{\text{ref}}^2$ are ± 0.0025 and 0.0025, respectively. The highest values of $\langle u'v'\rangle/U_{\text{ref}}^2$ actually occur in the vorticity layers of the vortex breakdown region, evident by comparison with the $\langle\omega\rangle$ contours of Fig. 3b. For the case of the stationary edge, these

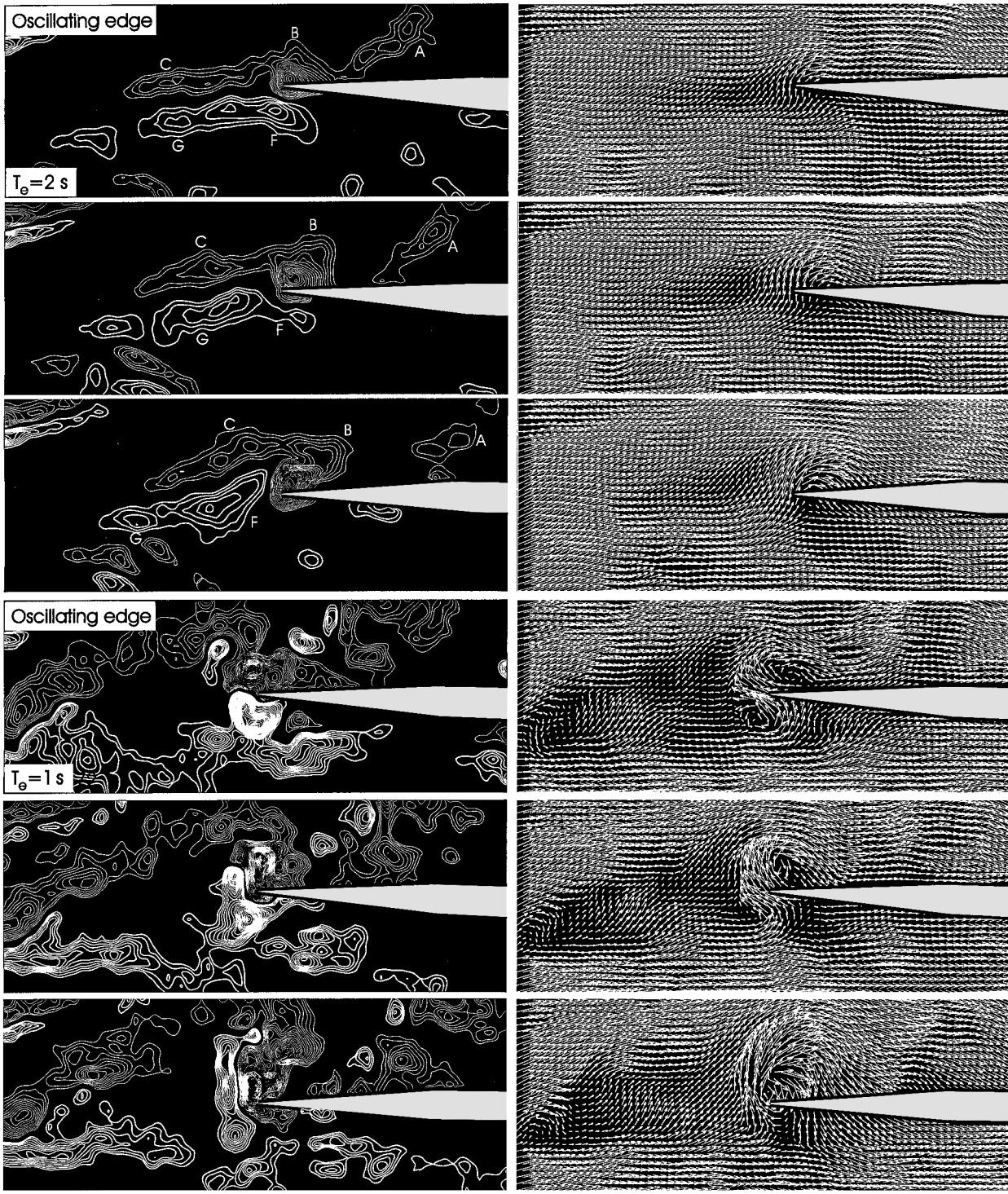

Fig. 4b Excerpts from cinema sequences showing patterns of instantaneous vorticity and distributions of velocity vectors for the case of an edge oscillating at T_e = 2 and 1 s.

peak values of $\langle u'v' \rangle / U_{\text{ref}}^2$ are, however, displaced downstream of the peak values of averaged vorticity $\langle \omega \rangle$. Distinguishing features of the case of the oscillating edge at $T_e = 6$ s are the relatively high levels of $\langle u'v' \rangle / U_{\text{ref}}^2$ generated at the tip and along the upper surface of the edge, in contrast to the case of the stationary edge. In fact, the important role of the edge oscillation in generating high values of $\langle u'v' \rangle / U_{\text{ref}}^2$ is evident at $T_e = 1$ and 2 s in Fig. 3d. At $T_e = 1$ s, large values of $\langle u'v' \rangle / U_{\text{ref}}^2$ are induced well upstream of the tip of the edge.

The intent of each of the averaged images given in Figs. 3a–3d is to provide an approximate reference image. Such an image is the consequence of the time sequence of instantaneous patterns, which is addressed in the next section. The effect of the number N of instantaneous images employed to obtain the averaged image is indicated in Fig. 3e for the vorticity $\langle \omega \rangle$ and the velocity correlation $\langle u'v' \rangle / U_{\text{ref}}^2$. The overall forms of the averaged patterns appear to converge relatively quickly; an exception appears to be the positive (thick white line) concentration of $\langle u'v' \rangle / U_{\text{ref}}^2$ immediately above the tip of the leading edge. This approximate convergence of the overall patterns for a very limited number of cycles is apparently due to the cyclic-repetitive nature of the patterns of vorticity and velocity and the absence of significant low-frequency fluctuations. Dye visualization over a large number of oscillation cycles showed that presence of the plate inhibited the usual low-frequency, streamwise excursions of vortex breakdown that occur in absence of the plate.

Instantaneous Flow Patterns

The exhibited averaged flow pattern upstream and at the edge, in Figs. 3a–3d, is of course a consequence of the time evolution of the corresponding instantaneous patterns. Key features of the instantaneous structure are given in Figs. 4a and 4b, which show pairs of vorticity–velocity images. The minimum and incremental values of instantaneous vorticity ω are ± 2 and 0.75 s^{-1}, respectively. Natural frequency of vortex breakdown is $T_0 = 1.66$ s. The development of instantaneous patterns of vorticity on the stationary edge is indicated in the set of three images at the upper left of Fig. 4a. Vorticity concentrations A and C–G all originate from the initial process of vortex breakdown upstream of the tip of the edge. On the other hand, concentration B is generated from the tip of the edge. Following the time evolution of these images, it is evident that vorticity concentrations A and C successively attempt to merge with concentration B as they pass above the edge. For the case of edge oscillation at a relatively long period $T_e = 6$ s, shown in the bottom three rows of images of Fig. 4a, the pattern of instantaneous vorticity concentrations along the upper surface of the edge again indicate interaction between vorticity concentration A originating from vortex breakdown and an elongated vorticity layer B, which has a high level of vorticity, originally formed from the tip of the edge. Along the lower surface, vorticity concentration E undergoes relatively rapid decrease in level of vorticity. Upstream of the tip of the edge, the overall pattern of instantaneous concentrations, C, F, and G, is analogous to the pattern D, F, and G corresponding to the stationary edge. In other words, the upstream influence of the oscillating edge is not significant, save for possible alteration of details of the vorticity concentration.

The corresponding distributions of instantaneous velocity for both cases of the stationary and oscillating edge, exhibited in the right column of Fig. 4a, show generally similar regions of large velocity defect due to the onset of vortex breakdown. The interface between the region of relatively large and low velocity corresponds to the locus of high vorticity in the corresponding patterns of vorticity. Moreover, analogous regions of high-velocity gradient in the vicinity of the tip of the edge again correspond to high vorticity.

Figure 4b shows, in the top three rows of images, the consequence of edge oscillation at $T_e = 2$ s. The patterns of instantaneous vorticity show that the onset of vortex breakdown has moved downstream substantially, and the width of the breakdown region, represented by the distance between layers of positive and negative vorticity, that is, between concentrations C and G, is relatively narrow. Moreover, the degree of agglomeration of vorticity into larger scale structures is not as pronounced as for the foregoing cases. The corresponding patterns of instantaneous velocity at $T_e = 2$ s shown in the right-hand column of Fig. 4b do not show a clearly identifiable region of low velocity that would indicate a pronounced wake defect due to onset of vortex breakdown. This remarkable retardation of the onset of vortex breakdown at $T_e = 2$ s corresponds to a value of $T_e/T_0 = 1.2$ in Fig. 2, which shows minimum values of $X_b^*/(X_b^*)_0 \cong 0.4$. The physical origin of this averaged retardation of the onset of vortex breakdown appears to be the compatibility between the edge oscillation and the arrival of incident concentrations of vorticity. This issue is further addressed in conjunction with Fig. 5.

At the smallest value of excitation $T_e = 1$ s, represented in the bottom three rows of Fig. 4b, the instantaneous structure of the positive and negative layers of vorticity takes on a fundamentally different form, relative to the preceding cases at larger T_e. It resembles a bubblelike mode of vortex breakdown. Moreover, small-scale concentrations of vorticity are embedded in these layers. At the tip of the edge, these incident layers appear to merge with pronounced concentrations of vorticity generated at the tip of the edge. Viewed as a whole, Figs. 4b suggest a close interrelationship between the pronounced concentrations of vorticity generated in the vicinity of the tip and the pattern of vortex breakdown well upstream of the tip. In essence, generation of large-scale vortices from the tip sets up an effective blockage. It is well known that the onset of vortex breakdown is highly sensitive to the scale of an obstacle placed in the flow. The vortex system at the tip, therefore, may be viewed as an equivalent obstacle that substantially advances the onset of vortex breakdown in the upstream direction. The corresponding patterns of

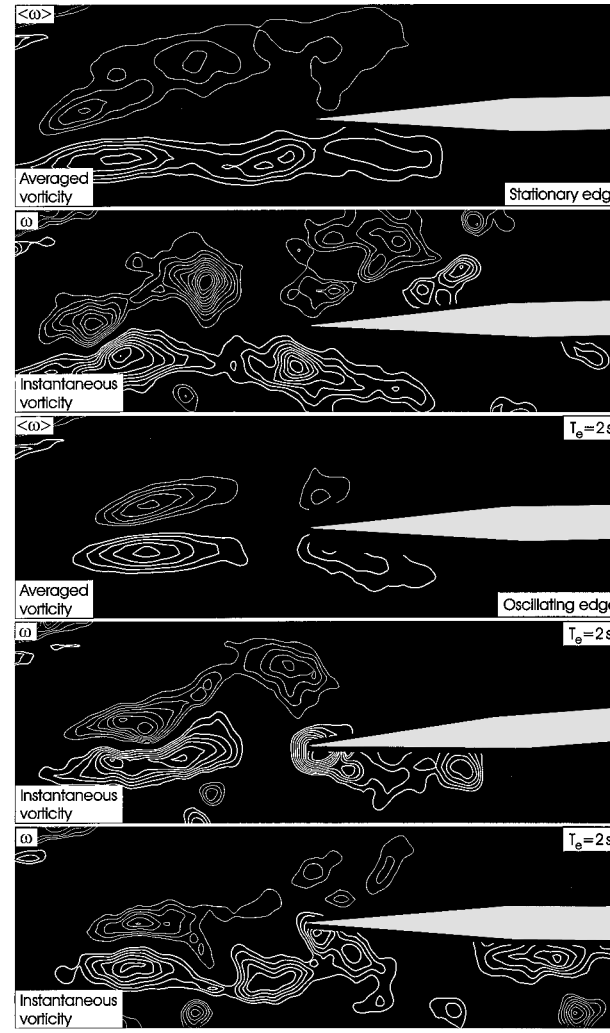

Fig. 5 Patterns of averaged and instantaneous vorticity for a stationary and oscillating leading edge. Angle of attack of delta wing is α = 24 deg.

instantaneous velocity shown in the right column indicate that the region of large velocity defect, associated with the onset of vortex breakdown, has moved considerably farther upstream than for the cases of the stationary edge and the edge oscillating at $T_e = 6$ s shown in Fig. 4a. Moreover, the pattern of relatively large-magnitude velocity vectors induced near the tip of the edge is compatible with the very high levels of vorticity concentration in that region.

The effect of angle of attack α_p of the plate was examined to ensure that the aforementioned retardation of the onset of vortex breakdown was a persistent feature. For the images shown in Fig. 5, the centerline of the plate is approximately aligned with the centerline of the region of vortex breakdown, corresponding to an angle of attack of the plate of $\bar{\alpha}_p = 2.5$ deg. As a consequence, as shown in the top two images of Fig. 5, leading-edge separation and the consequent generation of a vortex from the tip of the edge do not occur. The occurrence of a positive concentration of vorticity along the upper surface of the edge is simply due to clipping of the incident layer of positive vorticity during transverse undulations of the pattern of vortex breakdown. Generally, the patterns of instantaneous vorticity, which are indicative of the spiral mode of vortex breakdown, have a generally similar form relative to those in the top three rows of images of Fig. 4a. In Fig. 5, for both averaged and instantaneous images, the minimum and incremental values of vorticity are ± 2 and 0.75 s^{-1}, respectively.

For the case of edge oscillation at $T_e = 2$ s, the process of vortex breakdown is, again, substantially retarded in a manner similar to that represented by a pattern of average vorticity in Fig. 3b and instantaneous vorticity in Fig. 4b. The two instantaneous patterns at the bottom of Fig. 5 show instants corresponding to maximum negative and positive displacement of the edge. The important feature

of the interaction between the patterns of instantaneous vorticity and the oscillating edge is the relative position of the instantaneous large-scale cluster of vorticity relative to the position at the tip of the edge. In the first (upper) image of instantaneous vorticity at $T_e = 2$ s, the large-scale concentration of negative (thin line) vorticity is well above the tip of the edge, whereas in the second pattern of instantaneous vorticity, the large-scale concentration of positive (thick line) vorticity is well below the tip of the edge. This out-of-phase relationship between deflection of the edge and the arrival of incident concentrations of vorticity during a typical cycle of the edge oscillation appears to be a key factor that allows downstream movement, or retardation, of the vortex breakdown.

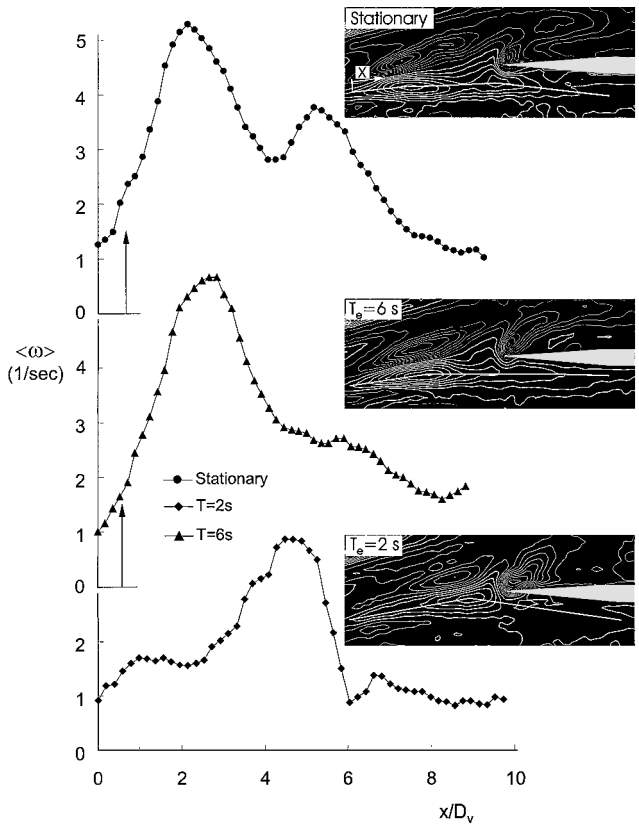

Fig. 6 Variation of averaged vorticity $\langle\omega\rangle$ as a function of dimensionless distance x/D_v.

Effect of Edge Oscillation on Averaged Swirl of Component of Vorticity of Incident Vortex

The averaged patterns of vorticity of the region of vortex breakdown provide, in essence, an indication of the effective, averaged strength of the swirl component of vorticity. That is, because the patterns of vorticity represent orientations normal to the plane of the image, and the laser sheet passes through the centerline of the vortex, distributions of the swirl component of vorticity are at hand. Figure 6 shows the variation of the peak value of averaged vorticity $\langle\omega\rangle$ as a function of distance along the vortex. Values of $\langle\omega\rangle$ are along the white line, corresponding to the locus of the vorticity extremum. As already suggested by Fig. 3b, and further shown in Fig. 6, the onset of vortex breakdown gives rise to extrema of averaged vorticity along the edge of the breakdown bubble, which appears to decay rapidly with increasing streamwise distance and for regions above and below the plate. To further emphasize this point, the variation of peak vorticity was considered along the white lines indicated in each of the respective images in the insets of Fig. 6. That is, these white lines correspond to the locus of peak vorticity along the lower portion of the vortex. The corresponding values of vorticity are represented by the three curves for the stationary edge and the oscillating edge at $T_e = 6$ and 2 s. Distance x is measured from the beginning of the white line, and the characteristic vortex diameter D_v corresponds to the transverse distance between the vorticity extrema in each pattern of vortex breakdown. For the case of the stationary edge, the peak vorticity rapidly attains its maximum value at $x/D_v = 2$, then exhibits decay, followed by a secondary peak, then further decay. For $T_e = 6$ s, a generally similar form of the curve is evident, except the secondary peak has been smoothed out by the effect of the oscillating edge on the pattern of vorticity in the vicinity of the tip of the edge. Finally, at $T_e = 2$ s, the onset of the peak value of vorticity is retarded to a location of approximately $x/D_v = 4.5$, followed by an abrupt decrease.

These variations of averaged vorticity are associated with changes in the instantaneous circulation Γ of the vorticity concentrations. Representative variations of $\Gamma/\pi D_v U_{\text{ref}}$ are shown in Fig. 7 for the case of the stationary edge. Three successive cycles of the incident pattern of vorticity concentration are considered, giving rise to concentrations $A1$, $A2$, and $A3$, as well as $B1$, $B2$, and $B3$. To provide a guide for interpreting these variations, three images at $N = 2$, 6, and 8 are shown for the first cycle of incident vorticity concentrations. The cluster of vorticity A_1 actually undergoes a substantial increase in circulation, apparently due to reorientation of the distribution of vorticity vectors along the edge of the separation bubble. The originally isolated concentration A_1 in image $N = 2$ evolves into an elongated form, with additional vorticity on either side of it. In image $N = 6$, and as is evident in image $N = 8$, the cluster of vorticity A_1 actually consists of three identifiable concentrations.

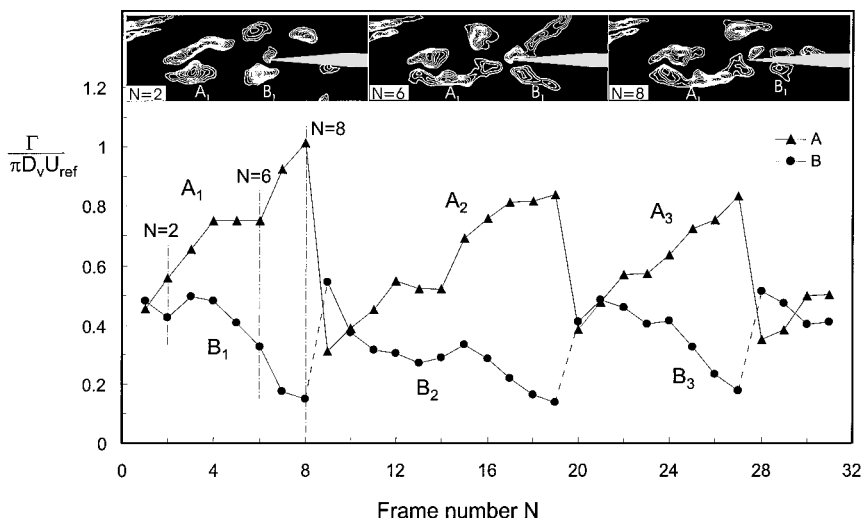

Fig. 7 Variation of dimensionless circulation Γ as a function of frame number N of a cinema sequence for representative, large-scale vorticity concentrations A and B.

At $N = 2$, B_1 is shown to have a relatively high peak vorticity and thereby circulation, and at successive instants, $N = 6$ and 8, it undergoes very substantial decrease in circulation as it encounters and moves along the surface of the edge. This attenuation is logical because the vorticity concentration is actually a cross section of the three-dimensional concentration associated with the spiral mode of instability and the leading edge represents an impermeable surface, which severs the incident spiraling vortex. Figure 7 shows the quantitative variation of dimensionless circulation. The pattern of increasing circulation associated with the cluster of vorticity A and the decreasing circulation of vortex B persists in a repetitive fashion over several cycles.

Spectra and Cross Spectra Based on Instantaneous Imaging of Vortex Breakdown–Edge Interaction

The cinema sequence of instantaneous images provides the possibility to construct spectra and cross spectra of time-dependent velocity components, as well as vorticity. The time interval between successive frames of the cinema sequence was $\Delta t = 0.18$ s, which corresponds to the sampling time. The corresponding value of the Nyquist frequency was $f_N = 2.78$ Hz. This value of sampling time Δt compares with the naturally occurring period of vortex breakdown, $T_0 = 1.66$ s. A total of 36 images was acquired over the time $T = 6.48$ s. This value of T corresponds to a bandwidth $B_e = 0.15$ cycles/s. Considerations for accurate calculation of spectra and cross spectra are defined by Newland.[28] Important is the acquisition of adjacent time records, which, when averaged together, can provide an increase in accuracy, relative to the case of a single record of duration T, irrespective of the length T of the original record. For the present experiment, such adjacent records were not obtained, and therefore, the calculated spectra and cross spectra must be viewed as approximate representations. The purpose of the present effort is to demonstrate the concept of calculation of spectra and cross spectra at a large number of spatial points over the flow domain using the same time record of sequential images from a cinema sequence. That is, the time variation of velocity and vorticity at each location (x, y) is equivalent to simultaneous acquisition of time records from a very large number of probes in the flow. Despite the foregoing approximations, the predominant frequency is correct within 5%, and the spatial variations of the spectra and cross spectra are in accord with what one expects from the larger scale vorticity concentrations.

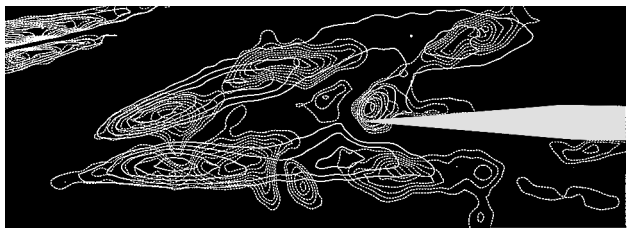

Fig. 8a Superposition of averaged (——) and instantaneous (- - -) contours of constant vorticity for a case of vortex breakdown incident upon a stationary edge.

The loading on the leading edge is a function of the frequency, amplitude, and phase variation of the flow patterns past the edge. To provide a guide for interpreting the spectra and cross spectra, the averaged distributions of vorticity $\langle\omega\rangle$ are employed. That these averaged patterns provide a reasonable representation of the loci of extrema of instantaneous concentrations of vorticity is evident from the comparison of Fig. 8a. It shows a superposition of averaged (solid line) and instantaneous (dashed line) vorticity for the case of the stationary edge. Examination of a series of these images from a cinema sequence shows that the instantaneous patterns of vorticity move through the averaged pattern. Minimum and incremental values of vorticity are ± 2 and 0.75 s^{-1}, respectively.

Figure 8b shows the averaged pattern of vorticity for the case of the stationary edge with a lower value of minimum vorticity than employed in preceding images. Also shown are corresponding spectra $S_u(f)$ of the streamwise velocity fluctuation u. The center image

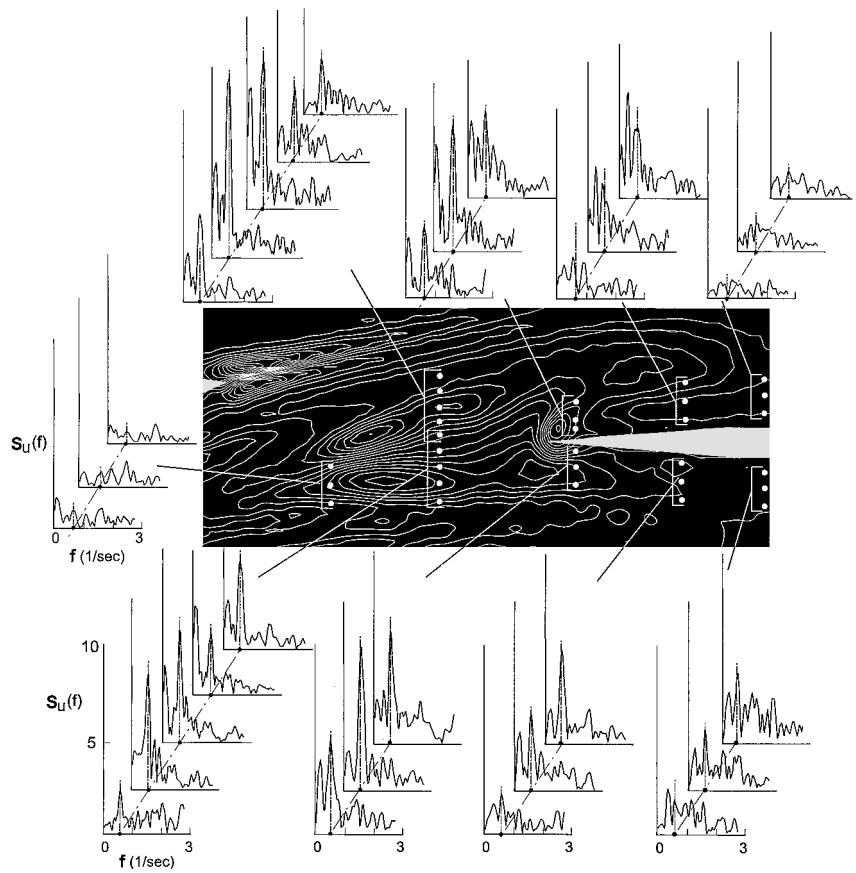

Fig. 8b Spectra $S_u(f)$ as a function of location in incident vortex breakdown and along surface of edge; frequency at which spiral mode of vortex breakdown occurs is $f = 0.6$ Hz.

shows the contours of constant averaged vorticity $\langle\omega\rangle$. The white dots indicate locations in the averaged vorticity pattern at which spectra were acquired. The three spectra on the left-hand side of the image represent a location near the onset of vortex breakdown, but just upstream of the location at which averaged and fluctuating vorticity become sufficiently large. It is evident that no sharply defined peak is evident in these three spectra. On the other hand, spectra taken downstream of the extrema of averaged vorticity indicate a sharply defined peak at $f_0 = 0.6$ Hz, corresponding to passage of the instantaneous vorticity concentrations suggested in Fig. 8a. The maximum amplitude of this spectral peak tends to occur near or at the location of maximum averaged vorticity in the corresponding image. At a location downstream of the tip of the leading edge, spectral peaks at the natural breakdown frequency $f_0 = 0.6$ Hz are again clearly evident. On the upper side of the tip of the leading edge, these peaks also correspond to the frequency of shedding of the tip vortex. Figure 8b also shows spectra at two locations farther downstream of the tip region. Spectra near the right boundary of the image exhibit a marked attenuation of their peaks. This observation corresponds to the decrease in dimensionless circulation of the vorticity concentrations along the surface of the leading edge, as addressed in Fig. 7.

Cross-spectral analysis was performed for the same cinema sequence as for Fig. 8b; the results are shown in Fig. 9. The components of the cross spectrum are 1) the magnitude $S_{ab}(f_0)$ corresponding to two locations a and b separated by distance Δs and 2) the phase shift $\phi_{ab}(f_0)$ at the same value of separation Δs. Values of $S_{ab}(f_0)$ and $\phi_{ab}(f_0)$ were determined as a function of distance downstream of the tip of the edge along lines designated as $1^+, 2^+, \ldots$ and $1^-, 2^-, \ldots$, above and below the edge surface respectively, for the transverse component of velocity v. Point a corresponds to the left edge of line 1^+ (and 1^- below the edge) and point b is located a distance Δs downstream of point a on line 1^+, 2^+, 3^+, or 4^+ for the region above the edge and similarly for the region below the edge. These values were determined over a rectangular grid of 16×7 points below the edge; the grid values were then interpolated to give contours of constant $S_{ab}(f_0)$ and $\phi_{ab}(f_0)$ shown in Fig. 9.

The magnitude of the cross spectrum $S_{ab}(f_0)$ in the region below the edge shows large values at the lower left corner of the plot

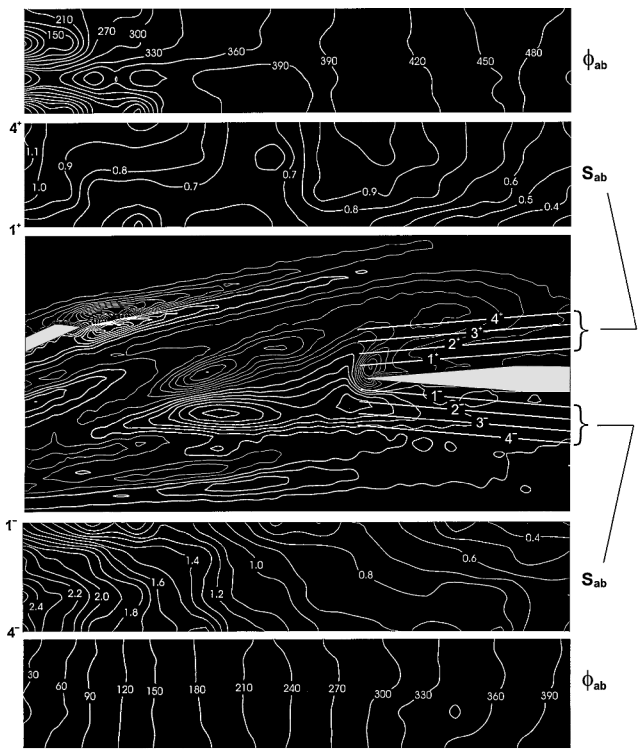

Fig. 9 Magnitude $S_{ab}(f)$ and phase $\phi_{ab}(f)$ of cross spectrum of transverse velocity fluctuation $v(t)$ for the case of vortex breakdown incident on stationary edge.

of constant contours of $S_{ab}(f_0)$. The magnitudes of these contours generally decrease in the streamwise direction. The physical basis for this type of distortion of contours of $S_{ab}(f_0)$ is the passage of instantaneous concentrations of vorticity through this region. They induce large amplitudes of the transverse velocity fluctuation $v(t)$, which yield large values of the magnitude of $S_{ab}(f_0)$. As these instantaneous patterns of vorticity move along the lower surface of the edge, the magnitude of their peak vorticity and correspondingly the peak values of velocity $v(t)$ decrease, contributing to relatively low values of $S_{ab}(f_0)$ over the right portion of the contours of constant $S_{ab}(f_0)$. Corresponding values of phase $\phi_{ab}(f_0)$ are given in the bottom plot of Fig. 9. The generally increasing values of ϕ_{ab} in the streamwise direction are in accord with the propagation of the aforementioned vortical patterns along the surface of the edge.

Above the edge, the patterns of $S_{ab}(f_0)$ and $\phi_{ab}(f_0)$ take on a more complex form, due to the localized formation of a vorticity concentration in the region immediately above the tip of the edge and, correspondingly, a distorted pattern of vorticity concentrations along its upper surface. These distortions are evident by examining the averaged contours of vorticity as shown in the middle plot of contours of constant $S_{ab}(f_0)$ above the edge; large values occur at the upper left corner, due to the process of tip vortex formation. Further distortions of the contours of $S_{ab}(f_0)$ are due to interactions between the incident vorticity concentrations rising from vortex breakdown and the concentrations associated with the tip vortex, as both move downstream of the tip region. This time sequence is indicated in Fig. 4a. As a result of these types of interactions, the contours of constant phase $\phi_{ab}(f_0)$ are distorted in the manner shown in the uppermost plot of Fig. 9. At locations sufficiently far downstream, the contours of constant phase $\phi_{ab}(f_0)$ take on a form more characteristic of a single row of propagating concentrations of vorticity.

Conclusions

Interaction of vortex breakdown with an oscillating leading edge gives rise to pronounced alterations of both the averaged and instantaneous structure of the incident, broken-down vortex and substantial distortion of the vortex in the region of the leading edge. The latter is influenced by vorticity generation at the tip of the edge. The principal findings are as follows.

Substantial retardation, or delay, in the onset of vortex breakdown and, thereby, development of large-scale concentrations of vorticity due to the helical mode of vortex breakdown are attainable when the leading edge is perturbed at a dimensionless time T_e (or frequency f_e) of the order of the corresponding timescale (or frequency) of the frequency of naturally occurring vortex breakdown. The physical origin of this retardation deserves further consideration. Possible mechanisms may be proper timing of the incident concentrations of vorticity relative to the motion of the tip of the edge and the phase shift of the distorted flow pattern along the surface of the plate.

On the other hand, remarkable advancement, that is, upstream movement, of the onset of vortex breakdown is attainable when the period of excitation of the edge T_e is sufficiently small, or correspondingly, the excitation frequency f_e is sufficiently large. In this case, pronounced concentrations of vorticity are formed along the upper and lower surfaces of the tip of the edge, thereby providing increased blockage for the incident vortex breakdown.

Averaged patterns of vorticity, which represent the azimuthal or swirling component, show development of pronounced extrema shortly downstream of the onset of vortex breakdown, then a rapid decay as the broken-down vortex moves past the leading edge. Root-mean-square distributions of fluctuating vorticity exhibit a pronounced extremum along the centerline of the broken-down vortex and at an axial location that is typically located downstream of the extremum of averaged vorticity in the shear layers along the breakdown bubble.

Distributions of Reynolds stress show extrema in the shear layers bounding the region of vortex breakdown; these extrema generally occur, however, at an axial location downstream of the extrema of averaged vorticity. In the case where substantial retardation of the onset of vortex breakdown occurs, the levels of Reynolds stress are negligible upstream of the tip of the edge. On the other hand, it is demonstrated that the presence of edge oscillation gives rise to very

high values of Reynolds stress in the vicinity of the tip of the edge. These levels are associated with vortex formation from the tip, and in the case of sufficiently low period T_e of the tip oscillation, that is, sufficiently high frequency f_e, regions of high Reynolds stress protrude well upstream of the tip.

Approximate values of spectra and cross spectra, evaluated from a time sequence of global images, show the transformation of the spectral content from the region of vortex breakdown upstream of the edge to the distorted breakdown along the surface of the edge. Pronounced spectral peaks are attenuated within a distance of six vortex diameters D_v downstream of the tip of the edge, such that broader-band background fluctuations exist in this region. Cross-spectral analysis in the vicinity of the tip of the edge provides portraits of both the cross-spectral amplitude and phase variations that dictate the effectiveness of loading of the surface of the edge.

Acknowledgments

The authors are grateful to the Air Force Office of Scientific Research for support of this investigation under Grant F49620-99-1-0011, monitored by Steven Walker. One of the authors, Besir Sahin, would like to thank the Scientific and Technical Research Council of Turkey and NATO for their financial support.

References

[1]Rockwell, D., "Vortex-Body Interactions," *Annual Review of Fluid Mechanics*, Vol. 30, 1998, pp. 199–229.

[2]Triplett, W. E., "Pressure Measurements on Twin Vertical Tails in Buffeting Flow," *Journal of Aircraft*, Vol. 20, No. 11, 1983, pp. 920–925.

[3]Brown, D., Lee, B. H. K., and Tang, F. C., "Some Characteristics and Effects of the F/A-18 Lex Vortices," *Vortex Flow Aerodynamics*, 494, AGARD, 1990, pp. 30-1–30-20.

[4]Lee, B. H. K., Brown, D., Zigela, L. M., and Poirel, D., "Wind Tunnel Investigation and Flight Tests of Tail Buffet on the CF-18 Aircraft," *Aircraft Dynamic Loads Due to Flow Separation*, CP-483, AGARD, 1990, pp. 1-1–1-26.

[5]Lee, B. H. K., and Brown, D., "Wind-Tunnel Studies of F/A-18 Tail Buffet," *Journal of Aircraft*, Vol. 29, No. 1, 1992, pp. 146–152.

[6]Huttsell, L. J., Tinapple, J. A., and Weyer, R. M., "Investigation of Buffet Load Alleviation on a Scaled F-15 Twin Tail Model," AGARD Structures and Materials Panel Workshop, Oct. 1997.

[7]Erickson, G. E., Hall, R. M., Banks, D. W., Del Frate, J. H., Schreiner, J. A., Hanley, R. J., and Pulley, C. T., "Experimental Investigation of the F/A-18 Vortex Flows at Subsonic Through Transonic Speeds, Invited Paper," AIAA Paper 89-2222, July–Aug. 1989.

[8]Fisher, D. F., Del Frate, J. H., and Richwine, D. M., "In-Flight Flow Visualization Characteristics of the NASA F-18 High Alpha Research Vehicle at High Angles of Attack," Society of Automotive Engineers, SAE Paper 892222, Sept. 1989.

[9]Del Frate, J. H., Fisher, D. F., and Zuniga, F. A., "In-Flight Flow Visualization and Pressure Measurements at Low Speeds on the NASA F-18 High Alpha Research Vehicle," NASA Ames Research Center, 1989.

[10]Sellers, W. L., Meyers, J. F., and Hepner, T. E., "LDV Surveys over a Fighter Model at Moderate to High Angles of Attack," Society of Automotive Engineers, TP Series Paper 88-1448, Oct. 1988.

[11]Komerath, N. M., Liou, S. G., Schwartz, R. J., and Kim, J. M., "Flow Over a Twin-Tailed Aircraft at Angle of Attack, Part I: Spatial Characteristics," *Journal of Aircraft*, Vol. 29, No. 3, 1992, pp. 413–420.

[12]Komerath, N. M., Liou, S. G., Schwartz, R. J., and Kim, J. M., "Flow Over a Twin-Tailed Aircraft at Angle of Attack, Part II: Temporal Characteristics," *Journal of Aircraft*, Vol. 29, No. 4, 1992, pp. 553–558.

[13]Breitsamter, C., and Laschka, B., "Turbulent Flow Structure Associated with Vortex-Induced Fin Buffeting," *Journal of Aircraft*, Vol. 31, No. 4, 1994, pp. 773–781.

[14]Mayori, A., and Rockwell, D., "Interaction of a Streamwise Vortex with a Thin Plate: A Source of Turbulent Buffeting," *AIAA Journal*, Vol. 32, 1994, pp. 2022–2029.

[15]Canbazoglu, S., Lin, J.-C., Wolfe, S., and Rockwell, D., "Buffeting of Fins: Distortion of Incident Vortex," *AIAA Journal*, Vol. 33, No. 11, 1995, pp. 2144–2150.

[16]Wolfe, S., Lin, J.-C., and Rockwell, D., "Buffeting at the Leading-Edge of a Flat Plate Due to a Streamwise Vortex: Flow Structure and Surface Pressure Loading," *Journal of Fluids and Structures*, Vol. 9, 1995, pp. 359–370.

[17]Beutner, T. J., Baust, H. N., and Meyers, J. F., "Doppler Global Velocimetry Measurements of a Vortex-Tail Interaction," *Proceedings of the 7th International Symposium on Flow Visualization*, edited by J. P. Crowder, Begell House, New York, 1995, pp. 418–423.

[18]Rizk, Y. M., and Gee, K., "Unsteady Simulation of Viscous Flow Field Around F-18 Aircraft at Large Incidence," *Journal of Aircraft*, Vol. 29, 1992, pp. 986–992.

[19]Gee, K., Murman, S. M., and Schiff, L. B., "Computational Analysis of F/A-18 Tail Buffet," AIAA Paper 95-3440, 1995.

[20]Kandil, O. A., Sheta, E. F., and Massey, S. J., "Buffet Responses of a Vertical Tail in Vortex Breakdown Flows," AIAA Paper 95-3464, 1995.

[21]Rizzetta, D. P., "Numerical Simulation of the Interaction Between a Leading-Edge Vortex in a Vertical Tail," AIAA Paper 96-2012, June 1996.

[22]Gordnier, R. E., and Visbal, M. R., "Numerical Simulation of the Impingement of a Streamwise Vortex on a Plate," AIAA Paper 97-17812, June–July 1997.

[23]Gordnier, R. E., and Visbal, M. R., "Numerical Simulation of the Impingement of a Streamwise Vortex on a Plate," *International Journal of Computational Fluid Dynamics*, Vol. 12, 1999, pp. 49–66.

[24]Garg, A. K., and Leibovich, S., "Spectral Characteristics of Vortex Breakdown Flowfields," *Physics of Fluids*, Vol. 22, No. 11, 1979, pp. 2053–2064.

[25]Gursul, I., "Unsteady Flow Phenomena Over Delta Wings at High Angle-of-Attack," *AIAA Journal*, Vol. 32, No. 2, 1994, pp. 225–231.

[26]Wolfe, S., Canbazoglu, S., Lin, J.-C., and Rockwell, D., "Buffeting of Fins: An Assessment of Surface Pressure Loading," *AIAA Journal*, Vol. 33, No. 11, 1995, pp. 2232–2235.

[27]Rockwell, D., Magness, C., Towfighi, J., Akin, O., and Corcoran, T., "High Image-Density Particle Image Velocimetry Using Laser Scanning Techniques," *Experiments in Fluids*, Vol. 14, 1993, pp. 181–19.

[28]Newland, D. E., *Random Vibrations, Spectral and Wavelet Analysis*, 3rd ed., Longman Group, Essex, England, U.K., 1993.

J. P. Gore
Associate Editor